CrystEngComm

ROYAL SOCIETY OF CHEMISTRY

PAPER

View Article Online
View Journal | View Issue



Cite this: *CrystEngComm*, 2020, **22**, 7066

# Room-temperature ultrafast synthesis, morphology and upconversion luminescence of $K_{0.3}Bi_{0.7}F_{2.4}$:$Yb^{3+}$/$Er^{3+}$ nanoparticles for temperature-sensing application†

Xiaoli Gao,[ab] Feng Song, *[ab] Dandan Ju,[c] Aihua Zhou, [d] Adnan Khan,[ab] Ziyu Chen,[ab] Xu Sang,[ab] Ming Feng[ab] and Lisa Liu[ab]

Received 23rd August 2020,
Accepted 12th September 2020

DOI: 10.1039/d0ce01231a

rsc.li/crystengcomm

An ultrafast route at room temperature has been developed for the first time to synthesize lanthanide ion ($Yb^{3+}$/$Er^{3+}$)-activated $K_{0.3}Bi_{0.7}F_{2.4}$ fluorescent nanoparticles and hold the potential to be applied in luminescent temperature sensors. In addition, the crystal structure and morphology of the $K_{0.3}Bi_{0.7}F_{2.4}$ nanoparticles prepared at different reaction conditions were studied in detail for the first time, including the reaction time and different mole ratios of Bi source and $NH_4F$. Moreover, $Yb^{3+}$/$Er^{3+}$ doped in the $K_{0.3}Bi_{0.7}F_{2.4}$ matrix using a luminescent thermometer based on the fluorescence intensity ratio technology was also investigated. Additionally, $K_{0.3}Bi_{0.7}F_{2.4}$:$Yb^{3+}$/$Er^{3+}$ revealed excellent up-conversion luminescence performance, and the up-conversion mechanisms of samples are affirmed according to the up-conversion emission intensity as a function of the pump power density. Simultaneously, the optical thermometric performance of the samples was investigated in the temperature range of 323–523 K to indagate the temperature sensor performance. Significantly, the maximum sensor sensitivity of the studied nanoparticles were 0.0058 $K^{-1}$ ($S_a$) at 523 K and 1.08 $K^{-1}$ ($S_r$) at 323 K, which indicates that $K_{0.3}Bi_{0.7}F_{2.4}$:20%$Yb^{3+}$/2%$Er^{3+}$ fluorescent nanoparticles can be exploited as a promising luminescent thermometer.



## 1. Introduction

Lanthanide ions ($Ln^{3+}$) activated up-conversion luminescence materials have been applied in many fields including three-dimensional displays, white light-emitting diodes, biological imaging, temperature sensors and photocatalysts because of their unique optical merits.[1–7] In particular, non-contact optical temperature sensing has attracted considerable attention in the past few years. Fluorescence intensity ratio (FIR) is regarded as the most promising approach for non-contact temperature detection because it is independent of the two thermally coupled levels of $Ln^{3+}$ ions as a function of the temperature in the measurement process.[8–10] Thereinto, the thermometric properties of $Er^{3+}$ activated up-conversion materials were largely investigated because of their thermally compound levels of $^2H_{11/2}$ and $^4S_{3/2}$ with proper energy separation in the range of 200–2000 $cm^{-1}$.[4] It was demostrated that various $Er^{3+}$-activated green emitting phosphors were proper FIR-based optical probers.[4] However, the sensor sensitivity is still not high enough and it needs to be addressed despite these advantages. Thus, we need to search for new optical thermometers to overcome these weaknesses. Moreover, the strong up-conversion luminescence is conducive to improving the accuracy of the temperature sensor.[11] Nevertheless, the fluorescence intensity is influenced by the host materials. Therefore, it is necessary to choose suitable host materials.[12]

It is known that the low phonon energy of an ideal matrix material can reduce the rate of non-radiative relaxation and maximize the luminous efficiency. During the past few decades, $Ln^{3+}$-doped fluoride as a research focus has attracted considerable attention. Because fluorides have good chemical stability and low phonon energy compared to other types of compounds, which is, therefore, often used as a matrix for effectively doping rare-earth ions.[13–15]

Bismuth is known as "green metal" with $[Xe]4f^{14}5d^{10}6s^26p^3$ electronic configuration because it possesses diverse oxidation states, multi-type electronic structures, nontoxic,

[a] *School of Physics, The Key Laboratory of Weak Light Nonlinear Photonics, Ministry of Education, Nankai University, Tianjin, 300071, PR China. E-mail: fsong@nankai.edu.cn*
[b] *Collaborative Innovation Center of Extreme Optics, Shanxi University, Taiyuan, Shanxi 030006, China*
[c] *School of Science, Tianjin Chengjian University, Tianjin 300384, PR China*
[d] *Physics Department, School of Science, Tianjin University of Science & Technology, Tianjin 300457, People's Republic of China*

† Electronic supplementary information (ESI) available. See DOI: 10.1039/d0ce01231a

and harmless properties.[16–19] Hitherto, we consider that $K_{0.3}Bi_{0.7}F_{2.4}$ may also be a suitable UC host material, which is inexpensive and thermodynamically stable at high temperatures. Until now, $K_{0.3}Bi_{0.7}F_{2.4}$ nanoparticles, as the bismuth-based host, are rarely reported for achieving $Ln^{3+}$ doping. Currently, for the $K_{0.3}Bi_{0.7}F_{2.4}$ samples, there is only one published paper on $Yb^{3+}/Tm^{3+}$ doped $K_{0.3}Bi_{0.7}F_{2.4}$ synthesized *via* a hydrothermal method as an UC luminescence material for deep-tissue optical imaging.[20] Thus, there is still no report on $Yb^{3+}/Er^{3+}$ co-doped $K_{0.3}Bi_{0.7}F_{2.4}$ matrix nanoparticles for temperature sensor applications. Moreover, $Yb^{3+}/Tm^{3+}$ doped $K_{0.3}Bi_{0.7}F_{2.4}$ were synthesized by a hydrothermal method in this study, and we did not study the matrix synthesis in detail. In our work, the $K_{0.3}Bi_{0.7}F_{2.4}$:$Yb^{3+}/Er^{3+}$ fluorescent nanomaterial was synthesized at room temperature and the morphology of the $K_{0.3}Bi_{0.7}F_{2.4}$ nanoparticles prepared under different reaction conditions are studied for the first time in detail, such as reaction time and different mole ratios of Bi source and $NH_4F$.

Herein, we report an ultrafast approach at room temperature to fabricate $x$%$Yb^{3+}$/2%$Er^{3+}$ activated $K_{0.3}Bi_{0.7}F_{2.4}$ luminescent nanoparticles based on a chemical precipitation method in 1 min. This method is simple, efficient and low cost without the application of high temperature and pressure environment. Besides, the crystal structure and morphology of the $K_{0.3}Bi_{0.7}F_{2.4}$ nanoparticles prepared under different reaction conditions are studied in detail. Moreover, the excitation and emission spectra of $Yb^{3+}/Er^{3+}$ doped $K_{0.3}Bi_{0.7}F_{2.4}$ UC nanoparticles reveal excellent luminescence performance. In addition, we also investigated the UC mechanism according to the UC emission intensity as a function of the pump power density. The temperature dependence of photoluminescence intensities for the $K_{0.3}Bi_{0.7}F_{2.4}$:20%$Yb^{3+}$, 2%$Er^{3+}$ sample was investigated at temperatures ranging from 323 K to 523 K. Furthermore, the potential application of the $K_{0.3}Bi_{0.7}F_{2.4}$:20%$Yb^{3+}$, 2%$Er^{3+}$ sample used as a temperature sensor was studied.

## 2. Experimental

### 2.1 Materials

KF (>99.9%), $NH_4F$ (>99.9%), $Bi(NO_3)_3{\cdot}5H_2O$(>99%) were purchased from Tianjin Damao Chem. Ethylene glycol (EG) and rear-earth reagents $Yb(NO_3)_3{\cdot}6H_2O$ (>99.99%), $Er(NO_3)_3{\cdot}6H_2O$ (>99.99%) were supplied by HWRK Chemical Company. All the reagents were of analytical grade and used without further purification.

### 2.2 Preparation of $K_{0.3}Bi_{0.7}F_{2.4}$ nanoparticles and $K_{0.3}Bi_{0.7}F_{2.4}$:20%$Yb^{3+}$, 2%$Er^{3+}$ nanoparticles

A room-temperature chemical precipitation method was used to synthesize the $K_{0.3}Bi_{0.7}F_{2.4}$ nanoparticles. First, 0.222 g $NH_4F$ was dissolved in a 25 mL EG solution under magnetic stirring in a 50 mL glass breaker. Then, 0.58 g KF and 0.485 g $Bi(NO_3)_3{\cdot}5H_2O$ were mixed into 10 mL of EG to form a homogeneous mixture. Whereafter, the $NH_4F$ solution was added to the above solution under magnetic stirring for different reaction times (1 min, 5 min, 30 min, 1 h, 3 h, and 6 h). Finally, the resulting white solid products were washed extensively three times with ethanol and dried at 80 °C for 12 h.

To prepare $K_{0.3}Bi_{0.7}F_{2.4}$:$x$$Yb^{3+}$/2%$Er^{3+}$ nanoparticles, KF (1 mmol), $Bi(NO_3)_3{\cdot}5H_2O$ (0.98–$x$ mmol), $Yb(NO_3)_3{\cdot}5H_2O$ ($x$ = 0.05, 0.1, 0.15, 0.2, and 0.25 mmol) and $Er(NO_3)_3{\cdot}5H_2O$ (0.02 mmol) were dissolved in 10 mL of EG. Then, a 25 mL $NH_4F$ solution was added to the above solution under magnetic stirring for 1 min. Finally, the products were washed extensively three times with ethanol and dried at 80 °C for 12 h.

### 2.3 Characterization

The crystal structure and purity of the as-synthesized $K_{0.3}Bi_{0.7}F_{2.4}$ were examined using a PANalytical X'Pert Pro diffractometer with Cu Kα radiation ($\lambda$ = 1.5406 Å) in the $2\theta$ range from 10° to 90° at 40 mA and 40 kV. The morphology and composition of the products were observed on a scanning electron microscope (SEM) (JEOL JMS-7500F) attached with an energy-dispersive X-ray spectrometer (EDX). Transmission electron microscopy (TEM) was performed using a Tecnai G2 F20. The Fourier transform infrared spectrum (FT-IR) of the sample was recorded on a TENSOR II FTIR spectrometer. The photoluminescence excitation and emission spectra and decay curves of samples were recorded using a Horiba Fluorolog-3 luminescence spectrometer equipped with a continuous 980 nm laser as the excitation source. Besides, the spectrum on $K_{0.3}Bi_{0.7}F_{2.4}$:20%$Yb^{3+}$/2%$Er^{3+}$ sample at the range of 323 K–523 K was recorded on a Nanolog luminescence spectrometer.

## 3. Results and discussion

The $K_{0.3}Bi_{0.7}F_{2.4}$ nanoparticles were synthesized using a chemical precipitation method at room temperature, and the corresponding schematic of the preparation process is shown in Fig. 1. The simple and facile synthetic method is suited for the fast production of $K_{0.3}Bi_{0.7}F_{2.4}$ nanoparticles, which is beneficial for practical production and applications.

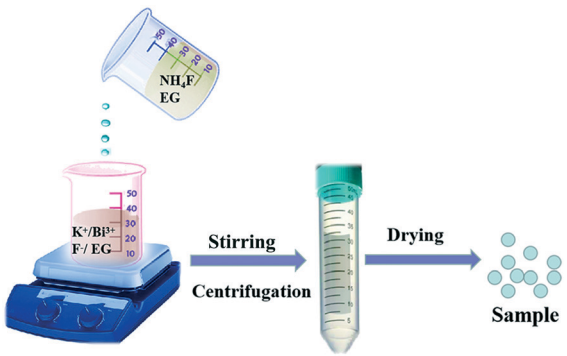


Fig. 1 Schematic for the preparation process for $K_{0.3}Bi_{0.7}F_{2.4}$ nanoparticles.

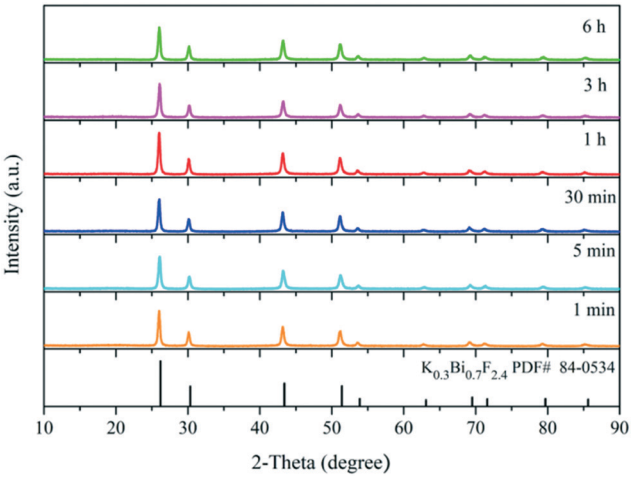


Fig. 2 XRD patterns of the $K_{0.3}Bi_{0.7}F_{2.4}$ samples prepared at different reaction times.

### 3.1 Phase identification and morphology of the $K_{0.3}Bi_{0.7}F_{2.4}$ products

To gain more information about the synthesis process, a series of time-dependent experiments were carried out to evaluate the influence of the reaction time on the structure of the $K_{0.3}Bi_{0.7}F_{2.4}$ sample with a constant concentration of $NH_4F$ (10 mmol) in the reaction system. As revealed in Fig. 2, strong and sharp diffraction peaks can be observed for the as-prepared samples obtained at different reaction times, and all the diffraction peaks could be indexed to the standard card data of $K_{0.3}Bi_{0.7}F_{2.4}$ (PDF#84-0534) without any trace of impurity phases, which demonstrate that the $K_{0.3}Bi_{0.7}F_{2.4}$ crystal can be produced in a short time of one minute, and the products possess high crystallinity and phase purity. The SEM images of the $K_{0.3}Bi_{0.7}F_{2.4}$ nanomaterials synthesized at different reaction times were recorded to observe the morphological evolution of products. As shown in Fig. 3 and S1,† the size distribution of the as-prepared nanoparticles is narrower and the average diameter is 50–60 nm. Moreover, there is almost no obvious difference in the morphology and size of the nanoparticles with the increase in the reaction time from 1 min to 1 h, even prolonging the reaction time to 3 and 6 h. The results indicate that the nucleation and growth of $K_{0.3}Bi_{0.7}F_{2.4}$ nanoparticles can be quickly completed because the thermodynamic effect can reduce the huge surface energy of nanoparticles to achieve equilibrium of the whole system energy.[21]

The XRD patterns plotted in Fig. 4 clearly show pure phase $K_{0.3}Bi_{0.7}F_{2.4}$ for all the products synthesized at different mole ratios of Bi source and $NH_4F$. In addition, when the mole ratio of the Bi source and $NH_4F$ is 1 : 1, the yield of the precipitate in the reaction system significantly decreases, implying that the synthesis of the $K_{0.3}Bi_{0.7}F_{2.4}$ is highly dependent on $NH_4F$.

In order to verify the aforementioned conjecture, a contrast experiment without using $NH_4F$ in the reaction solution was performed. We observed that precipitate is not generated in the solution after reacting for 6 h. The results demonstrate that $NH_4F$ plays a crucial role in the synthesis of $K_{0.3}Bi_{0.7}F_{2.4}$ nanoparticles and the phase purity of $K_{0.3}Bi_{0.7}F_{2.4}$ was not affected with the increase in the $NH_4F$ content.

Fig. 5 reveals the morphological evolution of $K_{0.3}Bi_{0.7}F_{2.4}$ samples prepared by regulating the Bi : $NH_4F$ molar ratio. It is found from Fig. 5a that $K_{0.3}Bi_{0.7}F_{2.4}$ samples obtained at a lower amount of $NH_4F$ (corresponding Bi : $NH_4F$ molar ratio of 1 : 1) are composed of smaller nanoparticles and the shape of the product presents quasispheres with a diameter of about 103 nm (Fig. S2a†), which is attributed to less nucleation due to the low concentration of $NH_4F$ in the

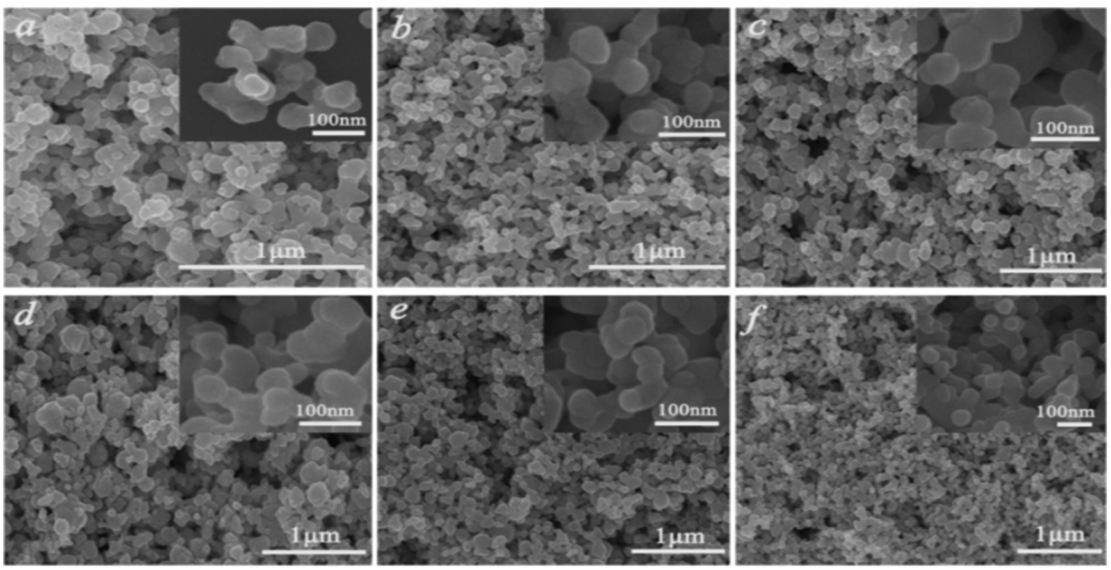


Fig. 3 SEM images of the $K_{0.3}Bi_{0.7}F_{2.4}$ samples at different reaction times. (a) 1 min, (b) 5 min, (c) 30 min, (d) 1 h, (e) 3 h, (f) 6 h.

 

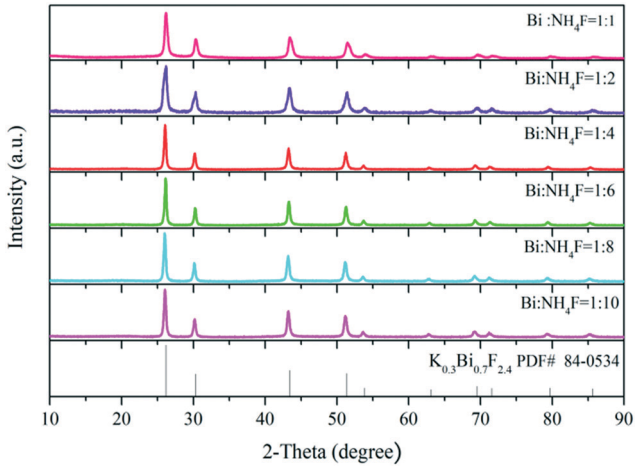


**Fig. 4** XRD patterns of the $K_{0.3}Bi_{0.7}F_{2.4}$ samples synthesized at a reaction time of 30 min with the different mole ratios of Bi source and $NH_4F$.

reaction system. At the Bi : $NH_4F$ molar ratio of 1 : 2, the scale of spherical-like nanoparticles reduces to about 85 nm (Fig. S2b†). For the samples prepared at a Bi : $NH_4F$ molar ratio of 1 : 4, the diameter of the spheroidal nanoparticles is approximately 76 nm (Fig. S2c†). With further addition of $NH_4F$ to the synthesis system (Fig. 5d), the size of the nanoparticles was about 66 nm (Fig. S2d†). When the Bi : $NH_4F$ molar ratios are 1 : 8 (Fig. 5e) and 1 : 10 (Fig. 5f), the mean diameter of $K_{0.3}Bi_{0.7}F_{2.4}$ decreases to 61 nm (Fig. S2e†) and 43 nm (Fig. S2f†), respectively. According to the experimental results, the change in the size of $K_{0.3}Bi_{0.7}F_{2.4}$ presents a downward trend with the increase in the mole concentration of $NH_4F$ in the synthetic system due to the nucleation number induced by the concentration of $NH_4F$. The results suggest that the presence of $NH_4F$ facilitates the preparation $K_{0.3}Bi_{0.7}F_{2.4}$ samples with a smaller size.

It is well-known that fluoride as a fluorescent host can diminish the quenching of activator ions to generate effective radiative transition, particularly for UC luminescence. Thus, the $Yb^{3+}/Er^{3+}$ activated $K_{0.3}Bi_{0.7}F_{2.4}$ nanoparticles with UC luminescence were synthesized.

The XRD patterns of as-synthesized $K_{0.3}Bi_{0.7}F_{2.4}$:$x$Yb$^{3+}$, 2%$Er^{3+}$ samples are illustrated in Fig. S3a.† It can be seen that all diffraction peaks of $K_{0.3}Bi_{0.7}F_{2.4}$:$x$Yb$^{3+}$, 2%$Er^{3+}$ crystals at different concentrations of $Yb^{3+}$ correspond well with the pure phase $K_{0.3}Bi_{0.7}F_{2.4}$ (PDF#: 84-0534). Fig. S3b† shows the photoluminescence emission spectra of $K_{0.3}Bi_{0.7}F_{2.4}$:$x$Yb$^{3+}$, 2%$Er^{3+}$ synthesized with different $Yb^{3+}$ concentration and 2% $Er^{3+}$. We note that the emission intensity of the samples increases at first with the increase in the $Yb^{3+}$ concentration and then decreases when $Yb^{3+}$ concentration reaches 20%. Hence, $K_{0.3}Bi_{0.7}F_{2.4}$:20%$Yb^{3+}$, 2%$Er^{3+}$ was selected in the subsequent experiments to study its luminescence characteristics and temperature sensing performance.

### 3.2 Phase identification, morphology and luminescence properties of the $K_{0.3}Bi_{0.7}F_{2.4}$:20% $Yb^{3+}$, 2%$Er^{3+}$ products

The structure, morphology, and UC luminescence properties of $K_{0.3}Bi_{0.7}F_{2.4}$ nanoparticles were first investigated using $Er^{3+}$ as an activator and $Yb^{3+}$ as a sensitizer. $K_{0.3}Bi_{0.7}F_{2.4}$:20%$Yb^{3+}$, 2%$Er^{3+}$ samples were

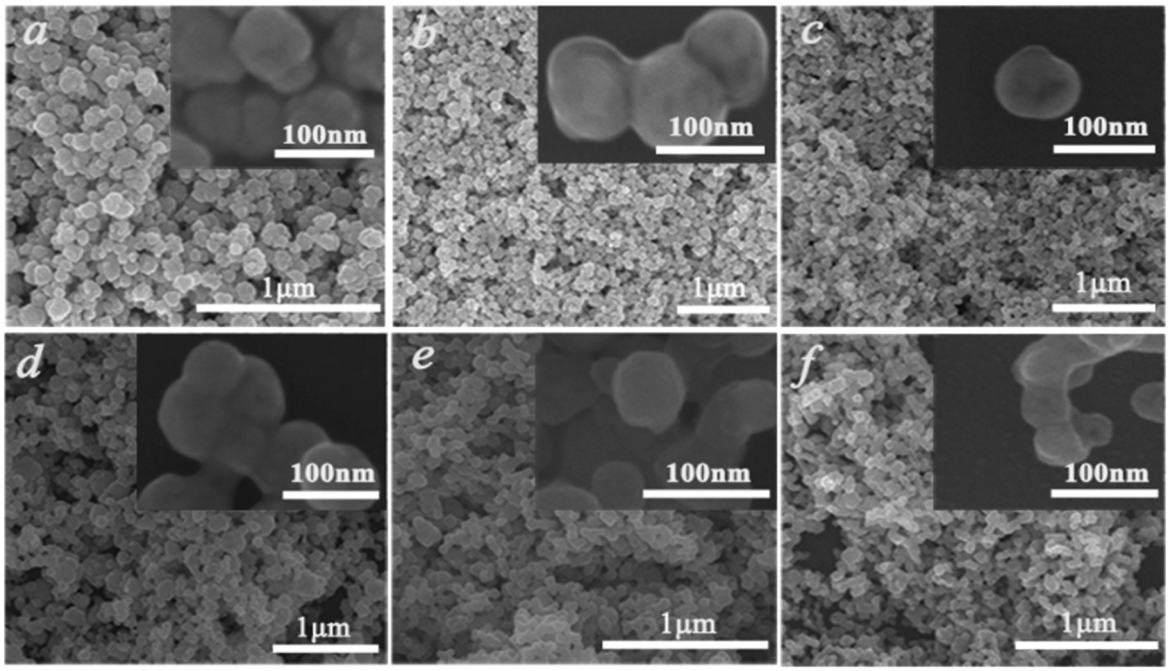


**Fig. 5** SEM images of the $K_{0.3}Bi_{0.7}F_{2.4}$ samples at different mole ratios of Bi source and $NH_4F$. (a) Bi : $NH_4F$ = 1 : 1, (b) Bi : $NH_4F$ = 1 : 2, (c) Bi : $NH_4F$ = 1 : 4, (d) Bi : $NH_4F$ = 1 : 6, (e) Bi : $NH_4F$ = 1 : 8, (f) Bi : $NH_4F$ = 1 : 10.

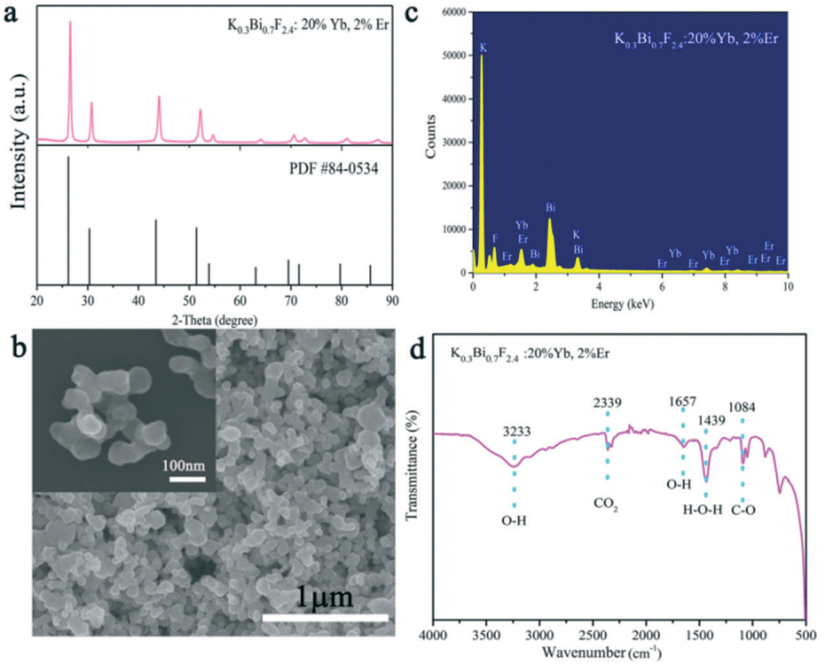


**Fig. 6** XRD patterns of the $K_{0.3}Bi_{0.7}F_{2.4}$:20%$Yb^{3+}$, 2%$Er^{3+}$ samples (a), SEM images (b), EDX spectrum (c), and FT-IR spectrum (d) of $K_{0.3}Bi_{0.7}F_{2.4}$:20%$Yb^{3+}$, 2%$Er^{3+}$ samples prepared at 1 min.

prepared under 1 min reaction time at room temperature using the chemical precipitation method. As exhibited in Fig. 6a, all the diffraction peaks of the samples obtained are well-defined with the crystal structure of $K_{0.3}Bi_{0.7}F_{2.4}$ (PDF#: 84-0534) with lattice parameters of $a = b = c = 5.89$ Å, $\alpha = \beta = \gamma = 90°$, $V = 204.34$ Å$^3$, and a space group of $Fm\bar{3}m(225)$. Fig. 6b reveals the SEM images of as-prepared $K_{0.3}Bi_{0.7}F_{2.4}$:20%$Yb^{3+}$, 2%$Er^{3+}$ samples in 1 min. With the doping of $Yb^{3+}$ and $Er^{3+}$ ions, the morphology of products is consistent with that of pure $K_{0.3}Bi_{0.7}F_{2.4}$ nanoparticles and maintains a relatively narrow size distribution. The results indicate that the introduction of $Yb^{3+}$ and $Er^{3+}$ as doped ions did not have a significant influence on the structure and morphology of the $K_{0.3}Bi_{0.7}F_{2.4}$ nanoparticles. To determine the element composition, the EDX spectrum (Fig. 6c) of $K_{0.3}Bi_{0.7}F_{2.4}$:20%$Yb^{3+}$, 2%$Er^{3+}$ nanoparticles was recorded. It can be seen that the chemical compositions of the as-synthesized samples include K, Bi, F, Yb and Er elements, and no impurity elements existed, suggesting that the $Yb^{3+}$ and $Er^{3+}$ ions are successfully doped into the $K_{0.3}Bi_{0.7}F_{2.4}$ host lattice. Furthermore, the FT-IR spectrum of the $K_{0.3}Bi_{0.7}F_{2.4}$:20%$Yb^{3+}$, 2%$Er^{3+}$ nanoparticles was recorded to confirm the existence of EG on the surface of nanoparticles. As displayed in Fig. 6d, the peaks located at 3233 $cm^{-1}$ and 1657 $cm^{-1}$ correspond to the stretching vibrations of the O–H. The sharp peak at 1439 $cm^{-1}$ and 1084 $cm^{-1}$ belongs to the H–O–H stretching vibration and C–O stretching mode, respectively. In addition, the characteristic absorption peaks at 2339 $cm^{-1}$ can be ascribed to the $CO_2$ derived from the surrounding environment.

Fig. 7a reveals the TEM image of the sample, which further verifies that the $K_{0.3}Bi_{0.7}F_{2.4}$:20%$Yb^{3+}$, 2%$Er^{3+}$ nanoparticles possess a spheroidal morphology. The high-resolution TEM (HRTEM) image of a selected area for $K_{0.3}Bi_{0.7}F_{2.4}$:20%$Yb^{3+}$, 2%$Er^{3+}$ nanoparticles presents a highly crystalline nature, which is consistent with the XRD results, as illustrated in Fig. 7b. The clear lattice fringes with an interplanar distance of 0.29 nm can be detected, which is in good agreement with the (200) plane of $K_{0.3}Bi_{0.7}F_{2.4}$.

Based on the HRTEM image of nanoparticles, a fast Fourier transform (FFT) pattern was obtained, which

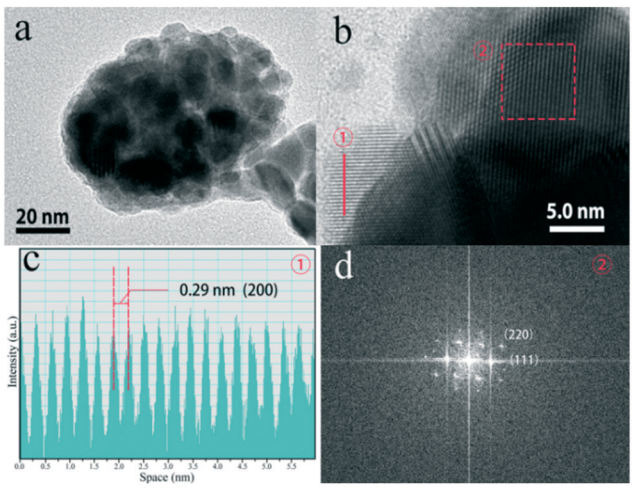


**Fig. 7** TEM images of the $K_{0.3}Bi_{0.7}F_{2.4}$:20%$Yb^{3+}$, 2%$Er^{3+}$ samples obtained at 1 min (a), HRTEM image (b), intensity plot of interlayer distance for the (200) plane (c) and FFT pattern (d).

 

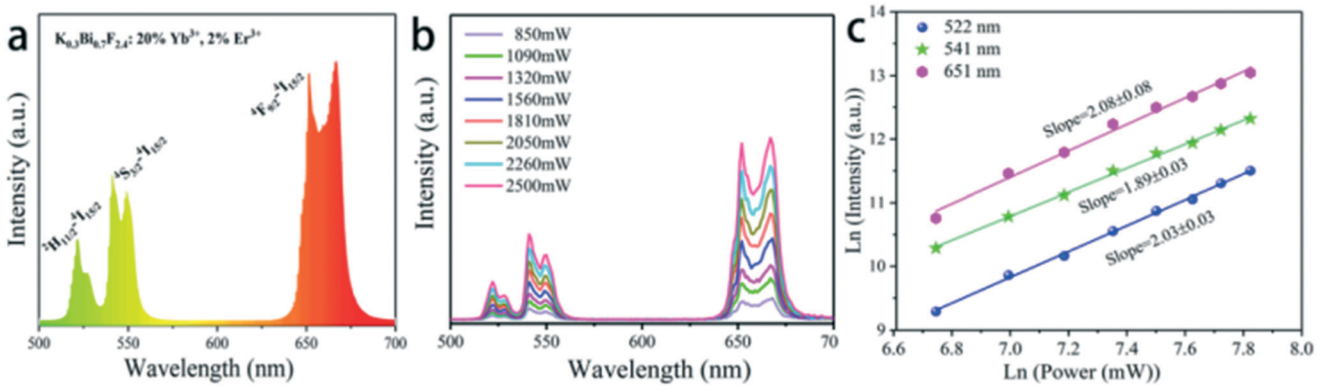


**Fig. 8** Photoluminescence emission spectra of (a) $K_{0.3}Bi_{0.7}F_{2.4}$:20% $Yb^{3+}$, 2% $Er^{3+}$ under 980 nm excitation, (b) UC emission spectra of the $K_{0.3}Bi_{0.7}F_{2.4}$:20% $Yb^{3+}$, 2% $Er^{3+}$ at the different pumping powers under 980 nm excitation, (c) Ln–Ln plots of the up-conversion emission intensity *versus* pump power for the $K_{0.3}Bi_{0.7}F_{2.4}$:20%$Yb^{3+}$, 2%$Er^{3+}$ nanoparticles under 980 nm laser radiation.

indicated a single-crystalline nature of the products and exhibited a well-defined structure with lattice fringe spacings of 0.21 and 0.34 nm corresponding to the (220) and (111) planes of $K_{0.3}Bi_{0.7}F_{2.4}$.

Fig. 8a shows the UC emission spectra of 20%$Yb^{3+}$/2%$Er^{3+}$ doped $K_{0.3}Bi_{0.7}F_{2.4}$ nanoparticles. Under 980 nm NIR excitation, the spectrum of $K_{0.3}Bi_{0.7}F_{2.4}$:20%$Yb^{3+}$/2%$Er^{3+}$ nanoparticles exhibits the typical UC emissions of $Er^{3+}$ ions. The result is consistent with previous literature.[20] Hereinto, the green UC emissions located at 522 and 541 nm originate from the transitions $^2H_{11/2} \rightarrow {}^4I_{15/2}$ and $^4S_{3/2} \rightarrow {}^4I_{15/2}$, respectively, and the red UC emission located at 651 nm corresponds to the $^4F_{9/2} \rightarrow {}^4I_{15/2}$ transition. To study the UC mechanism, we measured the UC luminescence of the samples under a series of excitation pump power (Fig. 8b). It is well known that the relationship between the UC emission intensity ($I_{em}$) of the samples and excitation pump power intensity ($I_P$) of the laser is expressed *via* the following formula: $I_{em} \propto I_P^n$, where $n$ is the number of pump photons absorbed in the UC process and can be calculated from the slope of the natural logarithmic plot.[22,23] The experimental data in Fig. 8c are fitted by the function Ln($I_{em}$) and Ln($I_P$), revealing that the slopes for $^2H_{11/2}$–$^4I_{15/2}$, $^2S_{3/2}$–$^4I_{15/2}$ and $^4F_{9/2} \rightarrow {}^4I_{15/2}$ ($Er^{3+}$, 522 nm, 541 nm, 651 nm) are 2.03 ± 0.03, 1.89 ± 0.03 and 2.08 ± 0.08 corresponding to two-photon (green and red) energy transfer processes. These results are consistent with previous reports.[24,25]

To clearly explain the UC mechanism, the detailed schematic energy level diagram and possible UC mechanism are shown in Fig. 9. Under the 980 nm laser diode excitation, the $^4I_{15/2}$ level of $Er^{3+}$ ions is excited to $^4I_{11/2}$ and $^4F_{7/2}$ levels by absorbing the energy from $Yb^{3+}$ ions. Then, the $^4F_{7/2}$ level nonradiatively relaxes to $^2H_{11/2}$ and $^4S_{3/2}$ states. Meanwhile, the $^2H_{11/2}$ and $^4S_{3/2}$ level can relax to the ground emitting green light near 522 nm and 541 nm.

Subsequently, the $^4I_{11/2}$ state of $Er^{3+}$ can also relax to $^4I_{13/2}$ and then populate to the $^4F_{9/2}$ energetic state by absorbing energy from $Yb^{3+}$. Finally, the $Er^{3+}$ in the $^4F_{9/2}$ state transfers to the $^4I_{15/2}$ state resulting in red light emission near 651 nm.[26,27]

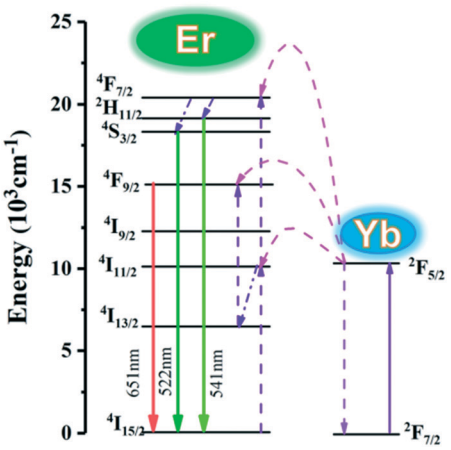


**Fig. 9** Energy level diagrams showing the UC of the $K_{0.3}Bi_{0.7}F_{2.4}$:20%Yb, 2%Er upon excitation at 980 nm.

### 3.3 Temperature sensing of samples

Aiming at exploring the probability of the thermometry application, the temperature sensing performance of the $K_{0.3}Bi_{0.7}F_{2.4}$:20%$Yb^{3+}$, 2%$Er^{3+}$ nanoparticles has been investigated. It is known that the energy gap of the $Er^{3+}$ between $^2H_{11/2}$ and $^4S_{3/2}$ states is about 750–850c $m^{-1}$.[28] Thus, the $^2H_{11/2}$ states can be populated from $^4S_{3/2}$ states because of the thermal coupling arising from this small energy separation. Finally, the emission intensity of $^2H_{11/2}$–$^4I_{15/2}$ and $^2S_{3/2}$–$^4I_{15/2}$ had variations under an elevated temperature. This characteristic indicates that $K_{0.3}Bi_{0.7}F_{2.4}$:20%$Yb^{3+}$, 2%$Er^{3+}$ may be applied in the temperature sensor using the FIR technique. Fig. 10a shows the normalized green emission spectra of $Er^{3+}$ ions by 980 nm excitation (laser power = 1.5 W) at the temperature range from 323 to 523 K. As plotted in Fig. 10a, it is clear that the emission intensity ratio of the $^2H_{11/2}$–$^4I_{15/2}$/$^2S_{3/2}$–$^4I_{15/2}$

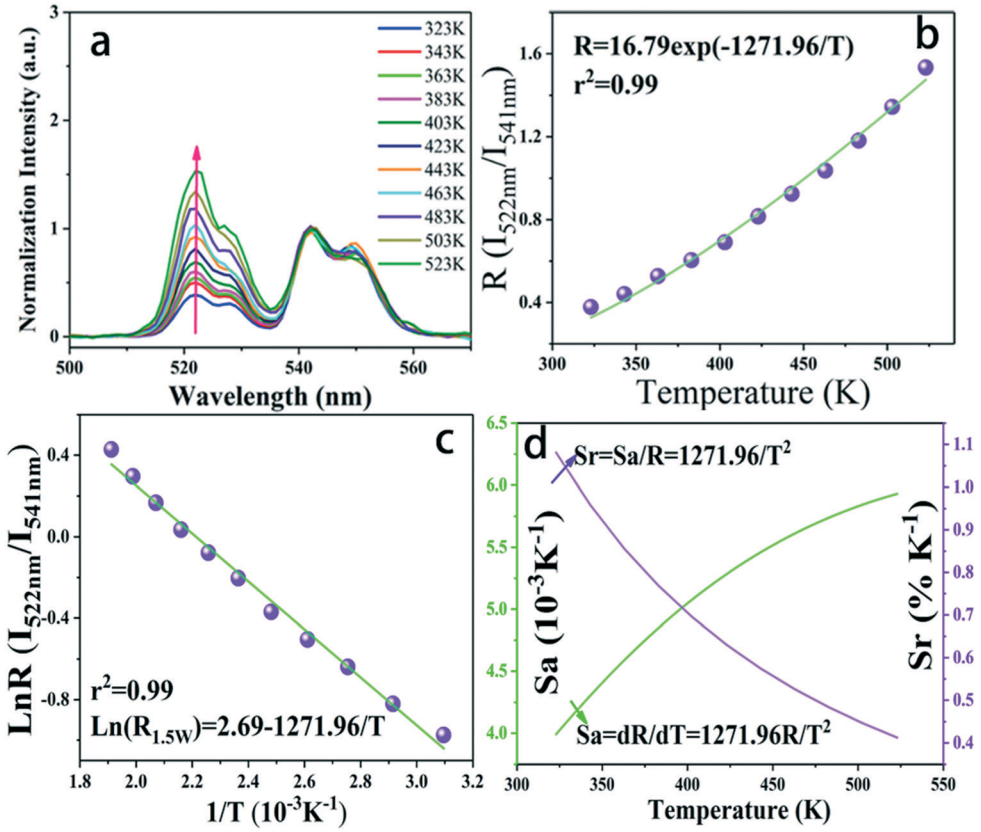


**Fig. 10** (a) Temperature-dependent normalized green emission spectra of $K_{0.3}Bi_{0.7}F_{2.4}$:20%$Yb^{3+}$, 2%$Er^{3+}$ nanoparticles under 980 nm excitation (laser power = 1.5 W). (b) Relationship between $R$ and the absolute temperature. (c) Monolog plots of Ln($R$) as a function of inverse absolute temperature. (d) The sensitivity of $K_{0.3}Bi_{0.7}F_{2.4}$:20%$Yb^{3+}$, 2%$Er^{3+}$ nanoparticle as a function of absolute temperature.

increases with the increase in temperature because of the Boltzmann-type distribution. According to the Boltzmann's equation, the fluorescence intensity ratio ($R$) can be defined as follows:[29,30]

$$R(I_{522nm}/I_{541nm}) = \frac{I_{522nm}}{I_{541nm}} = C\exp\left(-\frac{\Delta E}{k_B T}\right) \quad (1)$$

In which $I_{522nm}$ and $I_{541nm}$ denote the relative integrated intensities corresponding to $^2H_{11/2}$–$^4I_{15/2}$ and $^2S_{3/2}$–$^4I_{15/2}$ transitions, respectively; $\Delta E$ is the energy gap between the 522 nm and 541 nm; $C$ is the proportional constant; $k_B$ and $T$ are defined as the Boltzmann constant and the absolute temperature, respectively. It is noticeable that the intensity ratio $R(I_{522nm}/I_{541nm})$ and Ln $R(I_{522nm}/I_{541nm})$ can be well-fitted with relevant equations in Fig. 10(c) and (d) with good linear fitting degree values ($r^2$ value is 0.99). The slope and intercept values given by the linear fitting result are 2.69 and 1271.96, respectively. At last, the $\Delta E$ and constant $C$ are 0.11 eV and 16.79, respectively. Besides, sensitivity is also a significant parameter to evaluate the temperature sensing application. It is worth investigating, which can be determined by:[31–33]

$$S_a = \frac{dR}{dT} = R\frac{\Delta E}{k_B T^2} \quad (2)$$

Here, the calculated sensitivity values increased upon elevating the temperature to 523 K. The maximum sensitivity is about 0.0058 $K^{-1}$ at 523 K. Furthermore, compared to other results on previously developed optical thermometers, the $K_{0.3}Bi_{0.7}F_{2.4}$:20%$Yb^{3+}$, 2%$Er^{3+}$ nanomaterial has a relatively higher absolute sensitivity at 523 K. In addition, relative sensor sensitivity ($S_r$) at different temperatures was also discussed. Based on previous reports, the values of $S_r$ as a function of temperature were calculated by utilizing the following expressions:[33–35]

**Table 1** The comparison of maximum $S_a$, $S_r$ temperature sensing properties of Er-doped materials

| Compounds | $\lambda_{ex}$ [nm] | $T$ [K] | $S_a$ [$K^{-1}$] | $S_r$ [$K^1$] | Ref. |
|---|---|---|---|---|---|
| α-$NaLuF_4$:$Yb^{3+}$/$Er^{3+}$ | 980 | 150–298 | 0.0022 | — | 36 |
| CaZnOS:$Er^{3+}$ | 980 | 303–603 | 0.0033 | — | 37 |
| $NaBiF_4$:$Er^{3+}$/$Yb^{3+}$/$Fe^{3+}$ | 980 | 303–543 | 0.0053 | — | 38 |
| $Bi_4Ti_3O_{12}$:$Er^{3+}$ | 980 | 115–490 | 0.0043 | — | 39 |
| $KEr_3F_{10}$:$Er^{3+}$ | 980 | 303–573 | 0.00398 | — | 40 |
| $BiPO_4$:$Er^{3+}$/$Yb^{3+}$ | 980 | 313–573 | 0.00413 | 1.10% | 41 |
| BiOCl:$Yb^{3+}$, $Er^{3+}$ | 980 | 298–778 | 0.0028 | — | 42 |
| $Bi_3Ti_{1.5}W_{0.5}O_9$:$Er^{3+}$ | 980 | 83–423 | 0.00314 | — | 43 |
| $Na_{0.5}Bi_{0.5}TiO_3$:Er/Yb– | 980 | 93–613 | 0.0031 | — | 44 |
| Er, Yb:$GdVO_4$@$SiO_2$ | 980 | 297–343 | — | 1.01% | 45 |
| $K_{0.3}Bi_{0.7}F_{2.4}$:$Yb^{3+}$/$Er^{3+}$ | 980 | 323–523 | 0.0058 | 1.08% | This work |

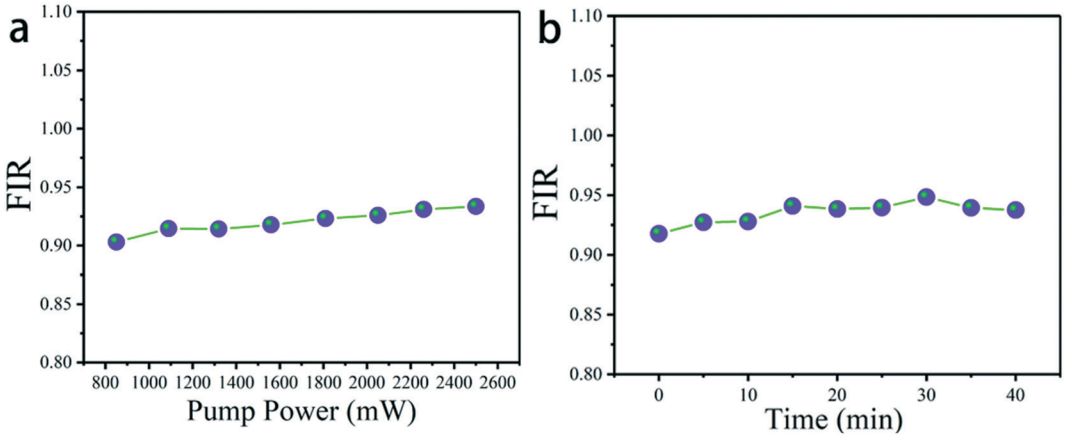


**Fig. 11** (a) FIR of the $K_{0.3}Bi_{0.7}F_{2.4}$:20%$Yb^{3+}$, 2%$Er^{3+}$ nanoparticles under 980 nm excitation at different power at room temperature, (b) FIR of the $K_{0.3}Bi_{0.7}F_{2.4}$:20%$Yb^{3+}$, 2%$Er^{3+}$ nanoparticles under 1.5 W (980 nm) excitation at persistent irradiation measured within 40 min.

$$S_r = \frac{1}{R}\frac{dR}{dT} = \frac{\Delta E}{k_B T^2} \quad (3)$$

As depicted in Fig. 10d, the corresponding resultant value of $S_r$ as a function of temperature has been given. In the detection range of 323–523 K, the value of $S_r$ monotonously decreases with temperature increases and the maximum value was about 1.08% $K^{-1}$ at the temperature of 323 K. Hence, the consequence implies that the sample may have potential applications in temperature sensing using the FIR technique. The temperature sensing properties of other Er-doped materials, which include fluorides, phosphate, vanadate and tungstate, are listed in Table 1.

Pump power and time-dependent up-conversion luminescence spectra of $K_{0.3}Bi_{0.7}F_{2.4}$:20%$Yb^{3+}$, 2%$Er^{3+}$ are plotted in Fig. 11a to verify the heating effect caused by 980 laser excitation. In addition, the luminescence spectra were recorded under 1.5 W (980 nm) excitation at persistent irradiation measured within 40 min in Fig. 11b.[45,46] As it can be seen that for the different powers of 980 nm excitation the value of FIR barely changed. Therefore, no pump induced heating is observed.[46] Furthermore, the value of FIR remained almost constant under persistent irradiation measured within 40 min, manifesting that the temperature of the material does not change greatly.

## 4. Conclusions

In summary, we have successfully developed an ultrafast synthetic strategy to prepare $K_{0.3}Bi_{0.7}F_{2.4}$ nanoparticles based on the facile chemical precipitation method at room temperature. The shape of the product is the spherical-like nanoparticles, and the average diameter of the samples decreased by regulating the mole ratio of the Bi source and $NH_4F$. However, the average diameter of the samples is no longer changed based on different reaction times. Furthermore, we have investigated the UC Photoluminescence properties and UC mechanism. In addition, this new $K_{0.3}Bi_{0.7}F_{2.4}$:20%$Yb^{3+}$, 2%$Er^{3+}$ phosphors could be used as a potentially useful temperature sensor utilizing the FIR technology due to the temperature-dependent property of $K_{0.3}Bi_{0.7}F_{2.4}$:20%$Yb^{3+}$, 2%$Er^{3+}$ phosphors revealing a linear relation at 323–523 K under 980 nm excitation and relatively high sensitivity.

## Conflicts of interest

There are no conflicts to declare.

## Acknowledgements

This work is financially supported by Natural Science Foundation of Tianjin, Key Project (no. 17JCZDJC37800) and National Natural Science Foundation of China (no. 11674183).

## References

1 S. Wu, X. Sun, Z. Meng and S. Zhang, *CrystEngComm*, 2017, **19**, 3600–3606.
2 X. Chen, C. Sun, S. Wu and D. Xue, *Phys. Chem. Chem. Phys.*, 2017, **19**, 8835–8842.
3 L. Liu, Y. Liang, L. Li, L. Zou and S. Gan, *CrystEngComm*, 2015, **17**, 7754–7761.
4 L. Luo, W. Ran, P. Du, W. Li and D. Wang, *Adv. Mater. Interfaces*, 2020, **7**, 1902208.
5 X. Li, M. Peng, J. Cao, Z. Yang and S. Xu, *J. Mater. Chem. C*, 2018, **6**, 7814–7821.
6 M. A. Antoniak, S. J. Zelewski, R. Oliva, A. Zak, R. Kudrawiec and M. Nyk, *ACS Appl. Nano Mater.*, 2020, **3**(5), 4209–4217.
7 P. Lei, R. An, X. Zhai, S. Yao, L. Dong, X. Xu, K. Du, M. Zhang, J. Feng and H. Zhang, *J. Mater. Chem. C*, 2017, **5**, 9659–9665.
8 D. Chen, Z. Wan and Y. Zhou, *Sens. Actuators, B*, 2016, **226**, 14–23.
9 F. Li, J. Cai, F. Chi, Y. Chen, C. Duan and M. Yin, *Opt. Mater.*, 2017, **66**, 447–452.
10 L. Tong, X. Li, J. Zhang, S. Xu, J. Sun, H. Zheng, Y. Zhang, X. Zhang, R. Hua, H. Xia and B. Chen, *Opt. Express*, 2017, **25**, 16047–16058.

11 R. Bao, N. An, L. Ye and L. Wang, *Opt. Fiber Technol.*, 2019, **52**, 101989.
12 G. Yi, H. Lu, S. Zhao, Y. Ge, W. Yang, D. Chen and L. Guo, *Nano Lett.*, 2004, **4**, 2191–2196.
13 S. Heer, K. Kömpe, H. U. Güdel and M. Haase, *Adv. Mater.*, 2004, **16**, 2102–2105.
14 L. Wang and Y. Li, *Chem. Mater.*, 2007, **19**, 727–734.
15 B. Zhou, B. Shi, D. Jin and X. Liu, *Nat. Nanotechnol.*, 2015, **10**, 924.
16 Y. Zhou, S. Ren, Q. Dong, Y. Li and H. Ding, *RSC Adv.*, 2016, **6**, 102875–102885.
17 P. Lei, P. Zhang, Q. Yuan, Z. Wang, L. Dong, S. Song, X. Xu, X. Liu, J. Feng and H. Zhang, *ACS Appl. Mater. Interfaces*, 2015, **7**, 26346–26354.
18 R. Mohan, *Nat. Chem.*, 2010, **2**, 336.
19 H. Li, R. Pang, G. Liu, W. Sun, D. Li, L. Jiang, S. Zhang, C. Li, J. Feng and H. Zhang, *Inorg. Chem.*, 2018, **57**, 12303–12311.
20 R. An, P. Lei, P. Zhang, X. Xu, J. Feng and H. Zhang, *Nanoscale*, 2018, **10**, 1394–1402.
21 P. Lei, R. An, S. Yao, Q. Wang, L. Dong, X. Xu, K. Du, J. Feng and H. Zhang, *Adv. Mater.*, 2017, **29**, 1700505.
22 H. Li, G. Liu, J. Wang, X. Dong and W. Yu, *Phys. Chem. Chem. Phys.*, 2016, **18**, 21518–21526.
23 R. Krishnan and J. Thirumalai, *New J. Chem.*, 2014, **38**, 3480–3491.
24 S. Ye, G. Chen, W. Shao, J. Qu and P. Prasad, *Nanoscale*, 2015, **7**, 3976.
25 G. Chen, H. Liu, G. Somesfalean, H. Liang and Z. Zhang, *Nanotechnology*, 2009, **20**, 385704.
26 H. Dong, L. Sun and C. Yan, *Chem. Soc. Rev.*, 2015, **44**, 1608.
27 L. Zhou, X. Zheng, Z. Gu, W. Yin, X. Zhang, L. Ruan, Y. Yang, Z. Hu and Y. Zhao, *Biomaterials*, 2014, **35**, 7666–7678.
28 J. Zhang, B. Ji, G. Chen and Z. Hua, *Inorg. Chem.*, 2018, **57**, 5038–5047.
29 A. Zhou, F. Song, Y. Han, F. Song, D. Ju and X. Wang, *CrystEngComm*, 2018, **20**, 2029–2035.
30 A. Zhou, F. Song, W. Yao, Y. Han, F. Song, W. Wu, C. Ming, D. Ju and A. Khan, *J. Alloys Compd.*, 2018, **775**, 457–465.
31 D. Chen, S. Liu, W. Xu and X. Li, *J. Mater. Chem. C*, 2017, **5**, 11769–11780.
32 P. Du, L. Luo and J. S. Yu, *J. Alloys Compd.*, 2015, **632**, 73–77.
33 J. Xue, H. Noh, B. Choi, S. Park, J. Kim, J. Jeong and P. Du, *Chem. Eng. J.*, 2020, **382**, 122861.
34 P. Du, L. Luo, H. Park and J. Yu, *Chem. Eng. J.*, 2016, **306**, 840–848.
35 P. Du, Y. Hou, W. Li and L. Luo, *Dalton Trans.*, 2020, **49**, 10224–10231.
36 L. Hao, D. Xu, A. Li, S. Yang and Y. Zhang, *J. Fluorine Chem.*, 2016, **192**, 41–47.
37 H. Zhang, D. Peng, W. Wang, L. Dong and C. Pan, *J. Phys. Chem. C*, 2015, **119**, 28136–28142.
38 P. Du, Q. Zhang, X. Wang, L. Luo and W. Li, *J. Alloys Compd.*, 2019, **805**, 171.
39 T. Wei, T. Zhang, Y. Ma, Y. Xie, C. Zhao, F. Yang, H. Xiao and Y. Zhao, *RSC Adv.*, 2016, **6**, 7643–7652.
40 P. Du, L. Luo, W. Li and Q. Yue, *J. Appl. Phys.*, 2014, **116**, 014102.
41 N. Wang, Z. Fu, Y. Wei and T. Sheng, *J. Alloys Compd.*, 2019, **772**, 371.
42 P. Du, L. Luo and J. S. Yu, *Microchim. Acta*, 2017, **184**, 2661.
43 Y. Zhang, J. Li, X. Chai, X. Wang, Y. Li and X. Yao, *J. Appl. Phys.*, 2017, **121**, 124102.
44 P. Du, L. Luo, W. Li and Q. Yue, *J. Appl. Phys.*, 2014, **116**, 014102.
45 J. Cai, L. Zhao, F. Hu, X. Wei, Y. Chen, M. Yin and C. Duan, *Inorg. Chem.*, 2017, **56**(7), 4039–4046.
46 A. Zhou, F. Song, F. Song, M. Feng, K. Adnan, D. Ju and X. Wang, *Opt. Mater.*, 2018, **78**, 438–444.

 